ELSEVIER

Contents lists available at ScienceDirect

# AdditiveManufacturing

journal homepage: www.elsevier.com/locate/addma



# Research paper

# Solid-stateproductionofuniformmetalpowdersforadditivemanufacturing byultrasonicvibrationmachining

Yaoke Wang<sup>a</sup>, Malachi Landis<sup>a</sup>, Clement Ekaputra<sup>b</sup>, Valeria Vita<sup>a</sup>, Ping Guo<sup>a,1</sup>

<sup>a</sup> Department of Mechanical Engineering, Northwestern University, Evanston, IL, USA <sup>b</sup> Department of Materials Science and Engineering, Northwestern University, Evanston, IL, USA



# ARTICLE INFO

Keywords:
Powder
Ultrasonic vibration machining
Additive manufacturing

# ABSTRACT

This work presents a new technique to generate uniform

and micron-sized metal powders for additive manufacturing. By collecting discrete chips resulting from ultrasonic vibration machining, we demonstrate the feasibility of all solid-state production consistent powders with tight dimensional tolerance, the ability to control powder geometry, and good efficiency. The technique offers a new route for sustainable and lowcost manufacturing of high-quality metal powders. The powder generation mechanism is analyzed with a special tool path design to ensure consistent dimensions over multiple cuts. An analytical model to predict the dimensions of produced powders under different cutting parameters is introduced. Aluminum and brass powders of different dimensions are produced, and the overall shear ratio that governs the deformation during the machining process is calibrated with the experimental results. The morphology consistency of produced powders is investigated over multiple hours of production, illuminating the role of tool wear on final powder shape. A high-efficiency powder collection system and a scalable solution for parallel production are proposed for the introduced technique. Additive manufacturing experiments (laser powder bed fusion) are conducted using produced A356 aluminum powders, demonstrating the printability of produced powders in additive manufacturing. The microhardness of the printed parts for five different process parameters is measured to be 45% higher than the raw material on average.

#### 1. Introduction

The substantial advancement of additive manufacturing in recent decades has made downstream industries, including feedstock production, an emerging field for research and development. For metal additive manufacturing applications, the high procurement and energy cost of feedstocks, mainly micron-sized metal powders, has become one of the most challenging factors constraining the growth of the market [1]. In addition, the demand for high-quality 3D printed parts puts forward higher requirements on the raw powder characteristics, including morphology, uniformity, and purity [2-4]. The need for low-cost, high-quality, and sustainable metal powders has led to the research of powder fabrication processes [5]. Gas atomization, as one of the mainstream production methods, provides highquality powders and feasibility for mass production [6-9]. Atomization processes involve the re-melting of metal ingots, which is energy-intensive and inefficient. Moreover, to achieve a narrow distribution of powder sizes, sieving operations are needed that can reduce the generation efficiency to typically between 10 and 20 percent [5]. Besides gas atomization, other concerns regarding the sustainability and resilience of metal additive manufacturing.

Research efforts have been made to explore alternative approaches to metal powder production. Solid-state production methods, especially mechanically-based processes, have the potential to provide comparable powder quality with significantly lower cost and energy footprint [15,16], with the ball milling processes [17,18] being the most representative. Using ball milling to produce metal powders with recycled machining chips has been demonstrated with a good production rate and low cost [19]. By manipulating the process parameters, such as ball diameter, rotation speed, and atmosphere [20,21], the morphology of the produced powders can be further refined. Powders can be dotted or reinforced with non-metallic elements [22]. Additionally, ball milling is dependent on the material to be powderized and the milling media [18]. Due to the natural randomness of the ball milling process, the dimensions of these mechanically generated powders are usually nonuniform and may form an undesirably wide size distribution [18]. Powders larger than the preferred size limit printing resolution, while over-refined small powders can cause excessive cohesion [23] and lead to spreadability problems

Received 15 August 2023; Received in revised form 6 January 2024; Accepted 18 January 2024 Available online 23 January 2024

2214-8604/© 2024 Elsevier B.V. All rights reserved.

atomization-based processes using water [10,11], plasma [12,13], and centrifuges [14] also fail to provide a narrow powder size distribution [6]. The high equipment cost for atomization-based processes requires industrial-scale production to be cost-effective [5], leaving small-batch, onsite production economically infeasible. From a life cycle perspective, it imposes

[24]. Therefore, powders are often sized to fit within a certain distribution, such as 20 to 50 µm for laser powder bed fusion (L-PBF) [25]. Direct production of powders within this well-controlled size range has the potential to increase powder production efficiency and yield by avoiding labor-intensive sieving required to fix otherwise unacceptable powder size distributions [5]. A feed

<sup>&</sup>lt;sup>1</sup> Correspondence to: 2145 Sheridan Road L286, Evanston, IL, 60208, USA. *E-mail address*: ping.guo@northwestern.edu (P. Guo).

modulation turning method has been reported to produce fine metal powders, but its production rate is limited by the low modulation frequency, typically below 200 Hz [26]. Previously demonstrated powder fabrication by mechanical machining has yet been able to deliver uniformly sized powders with controlled morphology at a competitive production rate.

To address the technical gap, we propose a new solid-state powder production method by collecting discrete chips resulting from ultrasonic vibration machining of metallic workpieces. A cylindrical turning operation adds one-dimensional ultrasonic vibration at the tool tip to the radial direction. The emphasis in this vibration-assisted machining process is shifted toward the generated chips as the delivered metal powders. The methodology is described in Section 2, with the proposed turning process introduced in Section 2.1. Specifically, the turning process is divided into alternating steps to realize a specific overlapping pattern of the vibration trajectory such that the powder dimensions are consistent despite the evolving machined surface topography. In Section 2.2, we introduce an analytical method to predict the dimensions of produced powders and discuss the possibility of generating separate powders with deep depth of cuts. By using the proposed process, the produced powders are non-spherical ribbons; the functionality of non-spherical powders has been demonstrated by several previous studies [27-31] for different additive manufacturing processes.

Various experiments have been conducted to characterize and validate the feasibility of the process and are described in Section 3. The analytical model from Section 2.2 is validated and calibrated for observed shear deformation in Section 3.1. Aluminum and brass powders are produced under various process parameters and exhibit uniform, ribbon-like morphology. A setup for scalable powder generation is described in Section 3.2 along with a demonstration of a high-efficiency powder collection system used to collect a total of 94 g of A356 aluminum powder. The effect of tool wear over multiple hours of powder production is clarified in Section 3.3, with consistent overall size remaining even after chipping of the diamond tool. Finally, the produced powders are successfully demonstrated with L-PBF in Section 3.4, using a layer height of 20 um to match the capability of spherical powders. Microhardness tests show an average hardness increase of 45% over the raw material, though directiondependent porosity of significant size can be found throughout the samples. The relative simplicity of the proposed method, requiring only a CNC motion stage, programmable spindle axis, and ultrasonic actuator, can produce powders from any machinable raw cylindrical feedstock. This technique may serve as a novel onsite production solution for specialized metal powder production without requiring expensive, inefficient atomization equipment or laborious post-processing.

## 2. Methodology for consistent powder generation

# 2.1. Consistent powder generation using vibration-assisted machining

Uniform metallic powders are generated during vibration-assisted machining by collecting the discrete machining chips. The cutting tool vibrates in the normal direction of the material surface while cutting along the surface. The resultant tool trajectory is shown in Fig. 1(a). If the vibration amplitude  $A_{mp}$  is larger than half of the depth-ofcut (DOC), non-overlapping dimples are produced on the machined surface. Because the tool exits the workpiece during each vibration, the chips are discrete and substantive, producing powders of consistent morphology and dimension uniquely determined by the process and material parameters. Each machined dimple corresponds to one generated powder; the powder production rate is therefore the same as the tool vibration frequency, which can be in the ultrasonic range. For continuous production, the process is implemented in a cylindrical turning configuration, as shown in Fig. 1(b). The tool vibrates with frequency  $f_R$  in the radial direction. If the spindle revolution per second  $f_C$  and the tool feed rate  $V_Z$  are constant, the generated dimples will form a spiral path on the machined surface.

For a single cut on a pristine cylindrical surface, the powders will be uniquely determined and consistent. However, when the surface is subject to

subsequent vibration machining, the distribution and geometry of the dimples are affected by existing surface textures, causing the generated powder geometry and size become inconsistent and unpredictable. Removing previous features by cutting the surface flat would remedy this problem but waste considerable time and material. Instead, we propose a strategy to achieve consistent and continuous powder generation over multiple cuts by consideration of existing machined surface features. We design an alternating dimple pattern as shown in Fig. 1(c). The dimples generated by the odd cuts (1st, 3rd, 5th, ...) and the even cuts (2nd, 4th, 6th, ...) are shown in blue and yellow circles, respectively. Within a revolution of a cut, the distance  $\mathcal D$  between dimples along the cutting direction can be calculated by:

$$f_{R}$$

$$D = 2\pi R \quad \text{(1)}$$

$$f_{C}$$

where R is the workpiece radius. The next revolution will shift the tool along the Z-axis by  $W_0$ . In the cutting direction, the dimple distances are the same but shifted by D/2 by keeping [32]:

$$f_c$$
 1  $f_R$  2 — =  $K$ + -, (2) where  $K$  is an integer.

Each sequential cut shifts the tool entry point by 2/2 along the cutting direction such that the valleys of the new dimples coincide with the peaks of the prior dimples. This is achieved by slightly decreasing the spindle speed during the retraction motion when the tool returns to the beginning of the workpiece for the next cut. The odd and even cuts form a special overlapped pattern such that the peak of the machined surface of the odd cut is the valley of the even cut and vice versa. As shown in Fig. 1(b), the surface generated by the second cut (blue) divides the machined surface of the first cut (yellow) into separate areas, which are also the peaks of the machined surface. The third cut will be at the same location as the first cut but deeper, cutting off the yellow areas and generating powders.

In Fig. 1(c), the corresponding locations of generated powders are shown in the green and red dotted boxes, the shape of which is approximately represented by a hexagon. Importantly, the discrete powders generated by each cut are independent while consistent in dimensions since the odd cut and even cut can be regarded as one single process interlaced. The powder morphology will converge to a consistent and stable state over repeated cuts. The red hexagon, which represents the powders produced by the even cut, overlaps with the powders generated by the odd cut (green hexagon). Due to a DOC difference between the two cuts, the powder produced by the two cuts forms a special three-dimensional tessellation, which overlaps in the overhead view shown in Fig. 1(c). The morphology and tessellation of the produced powders will be discussed in Section 2.2.

#### 2.2. Morphology of produced powders

We simulate the powder shape and dimensions considering the existing machined surface topography using the following process parameters shown in Table 1. The additional parameter  $R_i$  is the tool nose radius. The simulation

corresponds to a powder generated by the current cut. The surface morphologies of Figs. 2(a) and 2(b) are the same, only shifted such that the peaks and valleys interlace with each other. As a result, the powder dimensions are consistent for long-duration production.

The undeformed dimensions of the produced powders can be directly

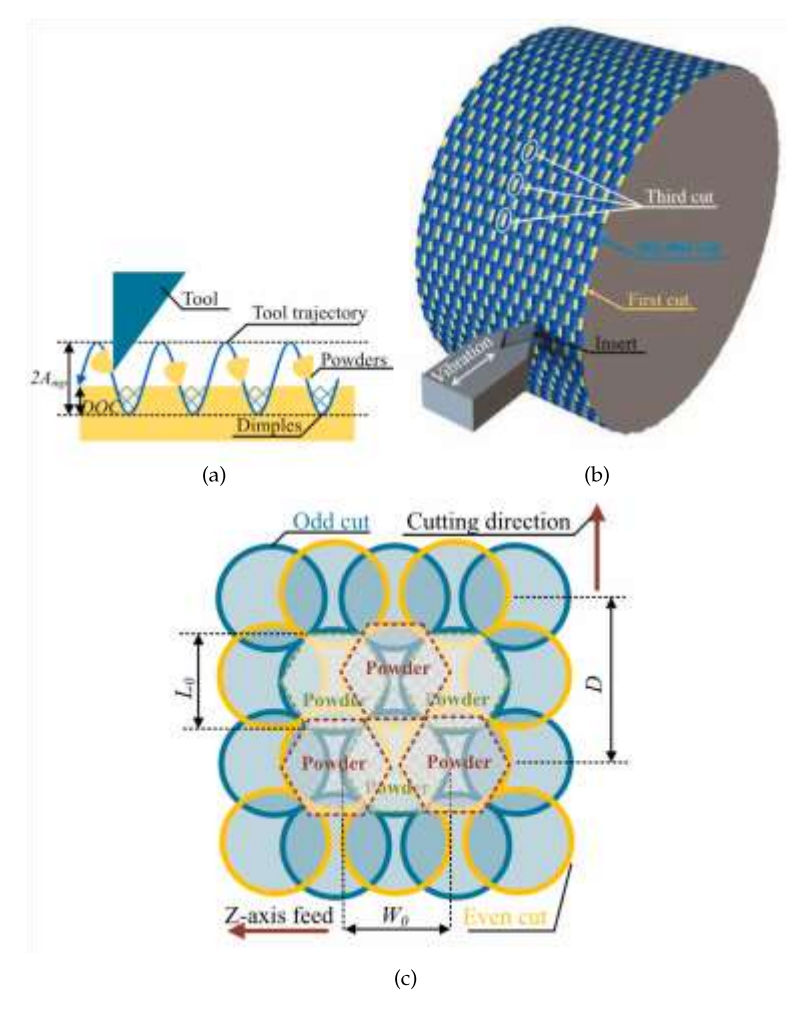


Fig. 1. (a) Powder generation by machining dimples with vibration cutting; (b) 3D representation of alternating cuts in turning operation; (c) alternating dimple pattern induced by odd and even cuts for consistent powder generation.

**Table 1**Summary of simulation parameters.

Summary of Simulation parameters.				
Spindle frequency	Workpiece radius	Nose radius	Feed	
<i>f<sub>R</sub></i> =11.50 Hz	R=35 mm	<i>R<sub>t</sub></i> =50,75,100 μm	F=50 μm	
Tool frequency	Vibration amplitude	Depth of cut	Dimple gap	
f <sub>c</sub> =25.8 kHz	<i>A<sub>mp</sub></i> =3.5 μm	<i>DOC</i> =0.25, 0.5,, 6.75 μm	<i>D</i> =100 μm	

model is based on our previous work [33] with a focus on the tool vibration-induced surface topography generation. As mentioned, the maximum  $\mathcal{DOC}$  is set to be smaller than the maximum depth of cut  $h_{max} = 2^{A}_{mp}$  to achieve non-connected powder generation. However, during the actual process, the  $\mathcal{DOC}$  can exceed  $h_{max}$  for certain conditions, which will be discussed in detail. There is a transition depth  $h_T$ , above or below which the dimensions of produced powders show different relationships with cutting parameters.  $h_T$  is usually smaller than  $h_{max}$  for most of the common tool geometry and cutting conditions. Thus, in this study, we focus on the conditions  $\leq$  where  $\mathcal{DOC}$   $h_{TT}$ ,  $h_{T} < \mathcal{DOC}$   $h_{max}$  and  $\mathcal{DOC} > h_{max}$ , respectively. The exemplary simulated surfaces and powders are shown in Fig. 2, where the initial and machined surface topography alternates between Figs. 2(a) and 2(b). Each dimple on the surface

obtained from the numerical simulation. For example, as shown in Fig. 2(c), the undeformed length  $L_0$ , width  $W_0$ , and thickness  $H_0$  of the powder are 166, 60, and 9.2  $\mu$ m, respectively, by using DOC = 6  $\mu$ m and  $A_{mp}$  = 3.5  $\mu$ m. If the DOC is significantly smaller than the amplitude and Z-axis feed ( $F = V I f_R$ ), the morphology of the produced powder converges to a curved rectangular chip, the  $L_0$ ,  $W_0$  and  $H_0$  of which are supposed to be D/2, F/2 and 2DOC, respectively. As shown in Fig. 2(d), when the DOC is 1  $\mu$ m instead of 6  $\mu$ m (other parameters are kept the same), the morphology of a produced powder is a curved rectangle. However, as the DOC increases, the morphology changes from a thin rectangle to an irregular ribbons presented in Fig. 2(c), resulting in the dimensions depending on the coupling of different cutting parameters, including dimple gap D, feed F, DOC, and vibration amplitude  $A_{mp}$ . Since the

dimensions of the produced powders are critical for the additive manufacturing process, the dimensions of the powders are required to be determined and controlled ahead of the production process. Several analytical models will be developed to succinctly capture the results of the numerical simulations and relate powder dimensions to process parameters.

As shown in Fig. 3(a), the cutting tool moves along the cutting direction

when  $DOC < h_{max}$ . To determine the undeformed width  $W_0$  and thickness  $H_0$ , it is necessary to investigate the section view of the process under each possible DOC condition.

Condition 1:  $DOC \le h_T < h_{max}$ 

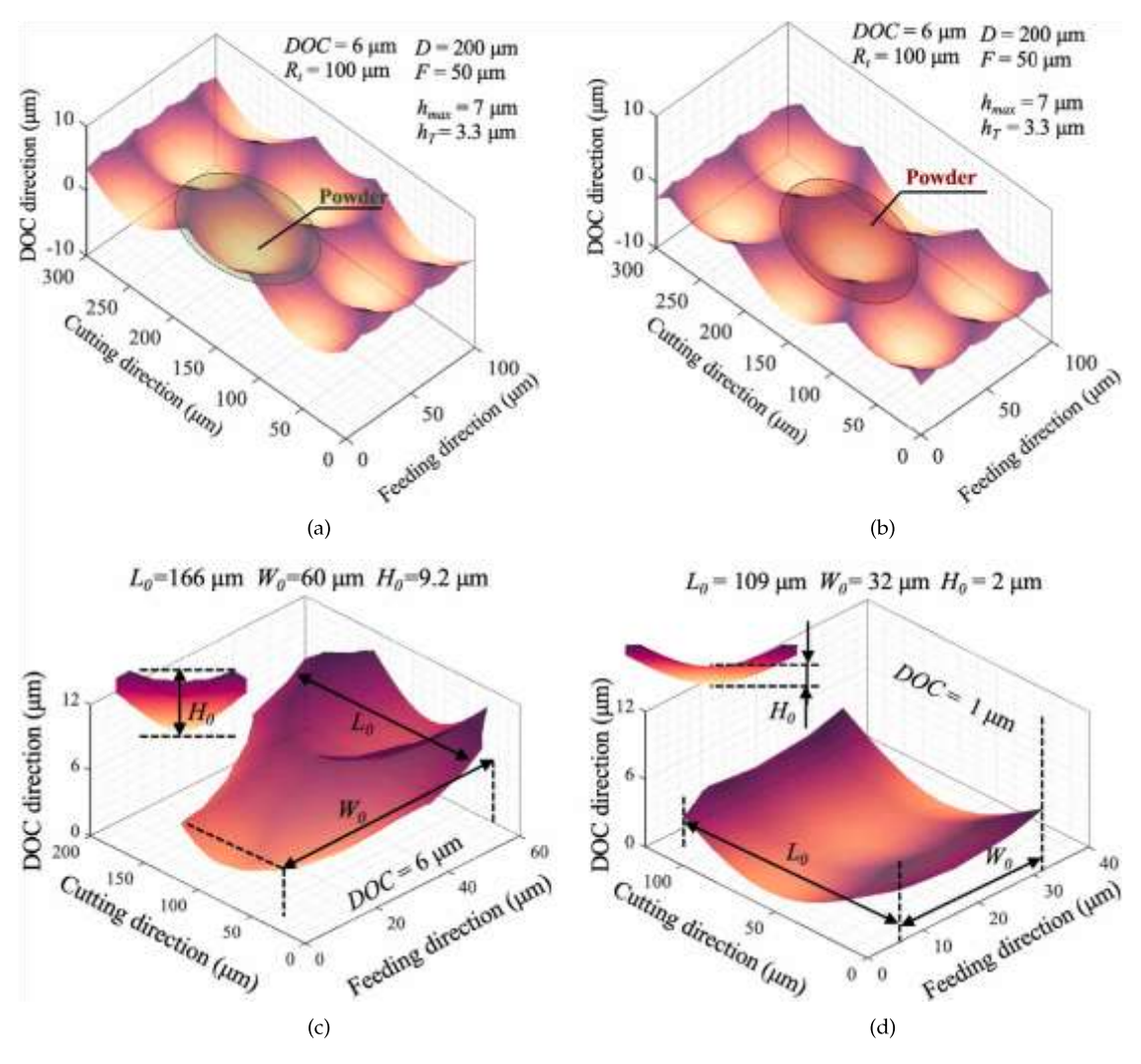


Fig. 2. The machined surface topography of (a) odd cut and (b) even cut; the theoretical shapes of corresponding generated powder when (c)  $\mathcal{DOC}$ =6  $\mu$ m and (d)  $\mathcal{DOC}$ =1  $\mu$ m. following the vibration trajectories of the odd cut (blue curve) and even cut (yellow curve). The phase difference between two trajectories is  $\pi$ , indicating that they are interlaced. Then within a period, the two trajectories have three intersections, forming two segments of different lengths. According to Fig. 3(a), the undeformed length  $L_0$  of the obtained powder is the length of the longer segment. By solving the intersection of the two vibration trajectories, the  $L_0$  can be calculated by:

$$\begin{bmatrix}
\begin{pmatrix} & & & \\ & DOC \end{pmatrix} \\
Z_0 = \begin{vmatrix} 1 & \frac{\arcsin \frac{m}{m}}{m} + \frac{2A}{m} \\
\end{vmatrix} = \frac{3}{m} + \frac{1}{m}$$

According to Eq. (3), when  $DOC \ll A_{mp}$ , the length  $L_0$  is equal to half of the dimple gap. When DOC is approaching  $h_{max} = 2A_{mp}$ , the length increases up to  $L_0 = D$ . When DOC exceeds  $h_{max}$ , the length is theoretically infinite, indicating a continuous chip generation instead of separate powders. Thus, Eq. (3) is valid

The section view of the dashed box in Fig. 3(a) is shown in Fig. 3(b), and the arcs in blue and yellow are the edge of the tool nose of odd and even cuts, respectively. The tool edges of the previous odd or even cuts are shown in dashed arcs, while the edges of the current cut are shown in solid lines. For a new cut, the cross-section of the resulting powder is the smallest independent area (not divided by other tool edges), searching from the lowest point of the current tool nose edge along the arcs of tool nose edges of all previous cuts. Intuitively, the section of the resulting powder of the current even cut is shown in the red dashed area in Fig. 3(b), which is enclosed by the arcs of the current cut, the two previous odd cuts, and the previous even cut. According to Fig. 3(b), the width  $W_0$  of the powder is the distance between the intersections of the current even cut and two previous odd cuts, which can be calculated using the geometrical constraints:

$$W^{0} = F_{+} \begin{vmatrix} \sqrt{V_{1} - V_{1} - V_$$

The thickness of the resulting powder is the gap between current and previous even cuts:

$$H_0 = 2 \cdot DOC.$$
 (5)

According to Eq. (4), the width of the produced powders increases as the  $\mathcal{DOC}$  increases, starting from  $\mathcal{F}/2$ . In addition, according to Eq. (5), the thickness is kept to twice the  $\mathcal{DOC}$ .

#### Condition 2: $h_T < DOC \le h_{max}$

As DOC increases, there is a critical depth of cut  $h_T$  where the intersection of the two previous odd cuts and the previous even cut

The thickness  $H_0$  of the resulting powder is the distance between the intersection of two previous odd cuts and the arc of the current cut:

$$H^{0} = R_{z} - \sqrt{R_{z}^{2} - \frac{F^{2}}{4}} + DOC.$$
 (8)

The tessellation styles of the powders from≤ Figs. 3(b) and 3(d) are clearly

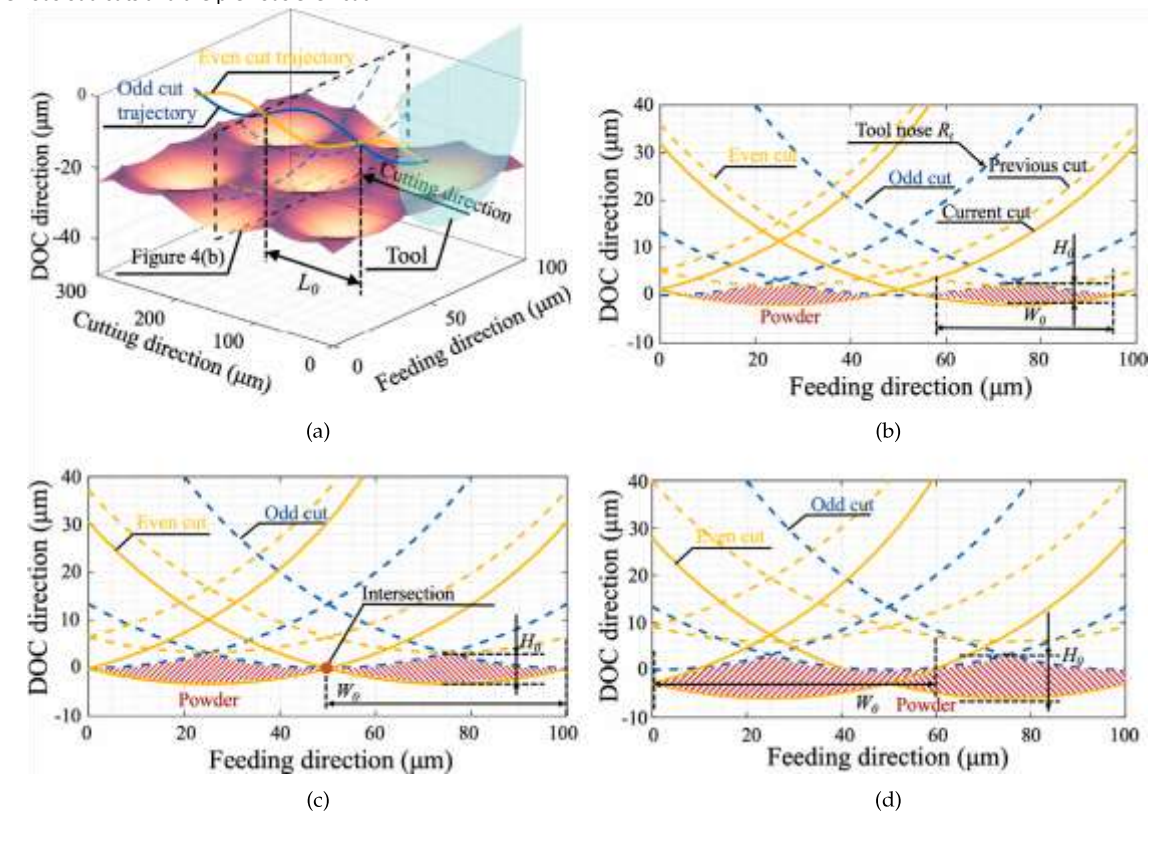


Fig. 3. (a) Surface morphology and tool trajectories; section view of the cutting process when (b)  $DOC < h_T$ , (c)  $DOC = h_T$  and (d)  $DOC > h_T$ . coincides, as shown in Fig. 3(c). Based on the given geometrical information,  $h_T$  different. When  $DOC / h_T$ , two adjacent powers be calculated by:

$$h_{T} = \frac{(-5\cancel{F}^{2} - 9\cancel{F}^{4} - 160\cancel{F}^{2}\cancel{A}_{i}^{2} + 256\cancel{A}_{i}^{4} + 16\cancel{A}_{i}^{2})}{-},$$

$$4 2$$
(6)

which is only related to the feed and the tool nose radius. In the example with parameters listed in Table 1,  $h_{max}$ = 2 $A_{mp}$ = 7  $\mu$ m and  $h_T$  equals 3.3, 4.5 and 7.8  $\mu$ m for 50, 75 and 100  $\mu$ m nose radius, respectively.

When DOC exceeds  $h_T(h_{T^{<}}DOC\ h_{max})$  as shown in Fig. 3(d), the section of the resulting powder is still enclosed by the arcs of the current even cut, two previous odd cuts, and the previous even cut but in a different sequence. As a result, the morphology of the resulting powder changes to be asymmetric. The width  $W_0$  is now the distance between the intersection of the current even cut with the previous even cut and the intersection of the current even cut with a previous odd cut. Based on this geometry,  $W_0$  is calculated as:

different. When DOC  $h_T$ , two adjacent powders produced in the even cut shown in Fig. 3(b) do not have a shared surface, and between them are the powders produced by an odd cut as shown in Fig. 4(a). When  $DOC > h_T$ , the two adjacent powders have a shared joint, the tessellation of which is shown in Fig. 4(b). In summary, regardless of the DOC condition below the uppermost limit, the proposed process forms a tessellation that provides consistent powder generation.

Numerical simulation results using the parameters in Table 1 are compared with analytical results provided by Eq. (3)–Eq. (8) and plotted together in Fig. 5. In the simulation, the tool nose radius  $R_\ell$  is set to be 50  $\mu$ m, 75  $\mu$ m, and 100  $\mu$ m, which refers to 1, 1.5, and 2 times the feed F. DOC changes from 0.3  $\mu$ m to 6.7  $\mu$ m, which gradually approaches  $h_{max}$ .

According to the comparison of the undeformed length  $L_0$  shown in Fig. 5(a), the numerical and analytical results are consistent.  $L_0$  is independent of  $R_t$ , indicating that the undeformed length of the powder is only dependent on the vibration amplitude  $A_{mp}$ , dimple gap D, and DOC. The width  $W_0$  shown in Fig. 5(b) increases approximately linearly with two different slopes as DOC increases. The transition point is exactly at the predicted  $DOC = h_T$ . When  $R_t = \frac{1}{2} \frac{$ 

50  $\mu m$ ,  $h_T$  is larger than  $h_{max}$ , causing  $W_0$  to increase with a constant slope in the simulation. The thickness of the produced powders starts to decrease from twice the DOC when  $DOC > h_T$ , as shown in Fig. 5(c), suggesting that increasing powder thickness by simply increasing DOC will give diminishing returns. According to the results in Fig. 5, it is feasible to use the aforementioned analytical solution to predict the threedimensional size of the produced powders instead of the numerical simulation.

#### Condition 3: DOC > hmax

When DOC exceeds the maximum depth  $h_{max}$  ( $DOC > h_{max}$ ), separate powders may still be generated. A simulation based on the same scheme is conducted by using  $DOC = 8 \mu m$  and  $h_{max} = 2 A_{mp} = 7 \mu m$ , the result of which is shown in Fig. 6. Under this condition, the long continuous chip can be regarded as separate powders connected by thin joints. The thickness of the thin joint is  $DOC - h_{max}$ , which may be bent and fractured due to shear deformation in the machining process. If all the thin joints break during the machining process,

separate powders will be obtained with an undeformed length equal to the dimple spacing  $\mathcal{D}$ . The width and thickness of such powders would still be calculated by Eqs. (7) and (8). The feasibility of powder production under this condition is verified in Section 3.1.

#### 3. Experimental verification

The powder production experiments are conducted on an ultraprecision lathe (Nanoform X, Precitech, USA) with linear axes (X and Z) and a programmable rotary axis (C). The details of the setup are shown in Fig. 7. The ultrasonic vibration is generated by a custom-designed ultrasonic vibration tool with a resonant frequency of 25.8 kHz and vibration amplitudes ranging from 1  $\mu m$  to 3.5  $\mu m$  [34]. Single crystal diamond (SCD) cutting inserts with nose radii of 74 and 107  $\mu m$  have been tested. During each cut, the ultrasonic tool feeds in the Z direction with an assigned DOC, generating powders following the proposed process. After each cut, the ultrasonic tool feeds a constant DOC in

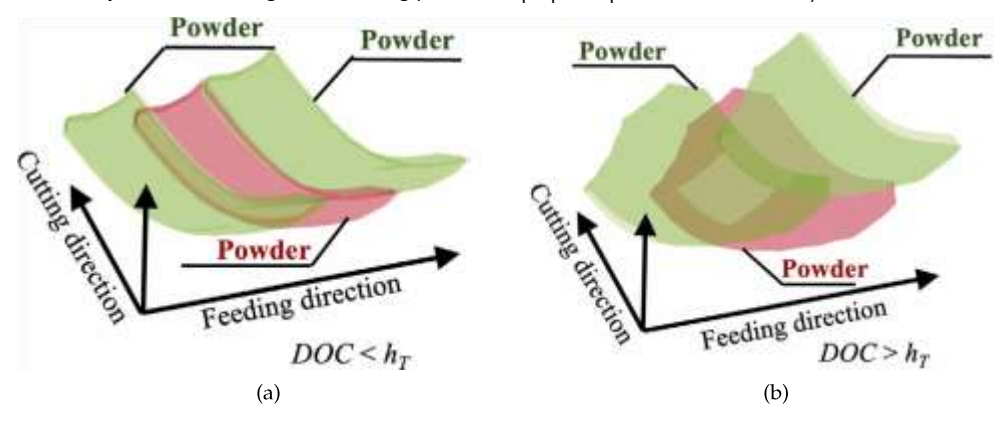


Fig. 4. Tessellation of powders in the cutting process when (a)  $DOC \le h_T$  and (b)  $DOC > h_T$ .

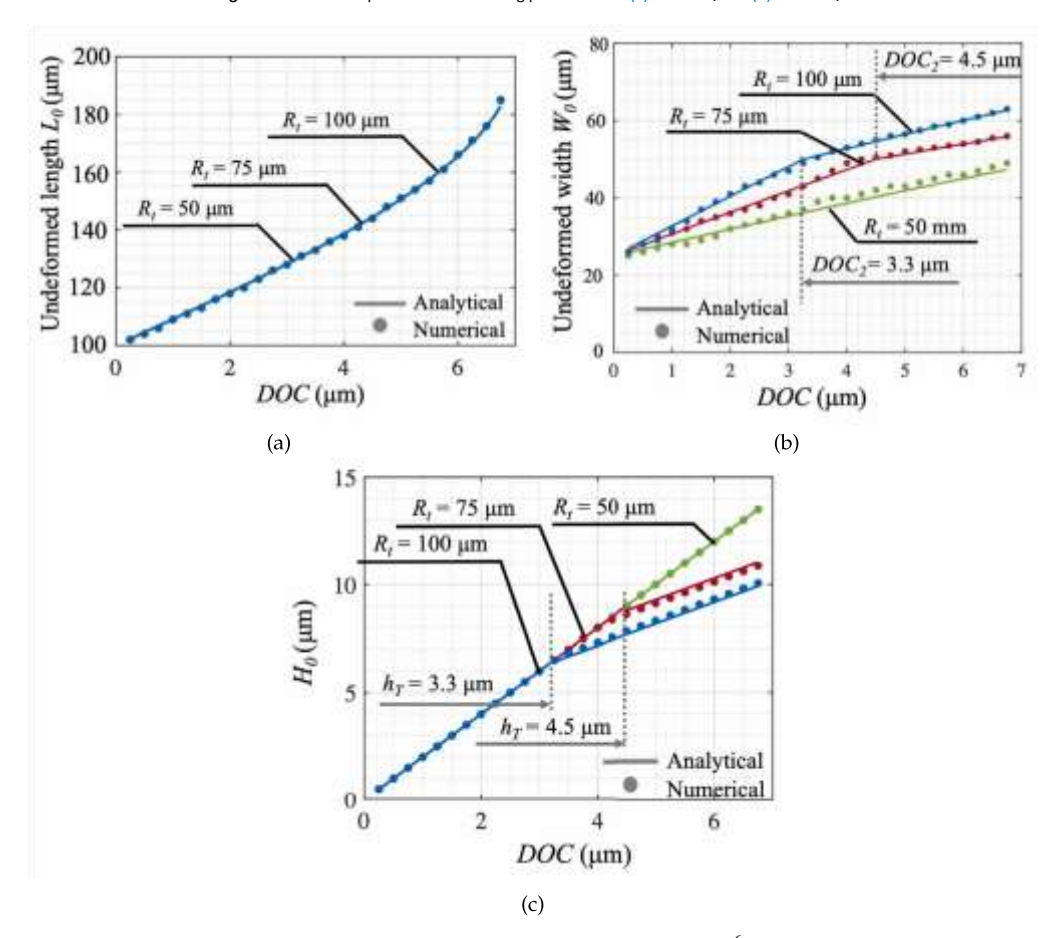


Fig. 5. The comparison of numerical and analytical simulation results of undeformed (a) length  $L_0$ , (b) width  $W_0$  and (c) height  $H_0$ .

the X direction and starts another cut. As the cutting process proceeds, the radius of the workpiece gradually decreases. To keep the powder length approximately constant when the diameter decreases, the program is updated for every certain period of production (in this study, the program is updated every 30 min). Here, the  $\mathcal{C}$ -axis is programmed with the position-time format to realize a precise angular gap between odd and even cut, which achieves the control of the entrance location for consistent powder generation.

width for the given parameters are 50  $\mu$ m by 40  $\mu$ m, nearly rectangular. The reason for this phenomenon is the shear deformation during the machining process, the effect of which requires further calibration.

Due to the shear deformation during the machining process, the length of the produced powder  $\it L$  decreases from the undeformed length Table 2

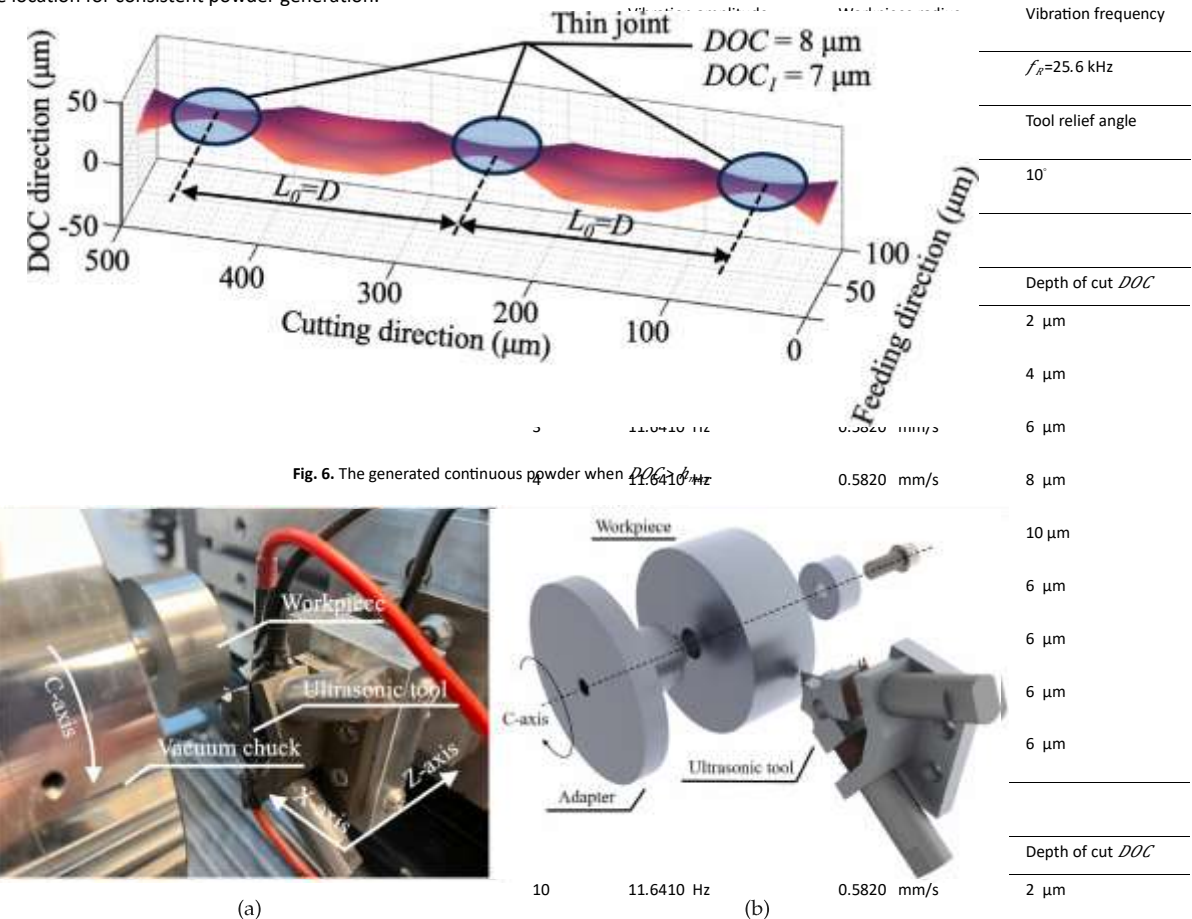


Fig. 7. (a) Experimental setup for powder generation; (b) 3-D models of ultrasonic tool and workpiece

#### 3.1. Verification of powder production

To verify the feasibility of the powder production method and investigate the shear deformation in the powder generation, including the prediction of dimensions, the feasibility of the  $\mathcal{DOC}$  in Section 2.2, 18 sets of experiments were conducted using the setup shown above, the parameters of which are listed in Table 2. The parameters in Table 2 aim to investigate the produced powders by changing dimple gap  $\mathcal{D}$  and  $\mathcal{DOC}$ , respectively.

The generated powders were directly collected on carbon tapes with aluminum substrates for SEM imaging. The image of the collected samples is shown in Fig. 8(a), where six sets of exemplary SEM results are shown in Figs. 8(b)–8(g). The brass powders tend to appear more pristine, with smooth edges, while the aluminum powders tend to have rougher or ragged edges. In Test 14, powders were produced in the  $DOC > h_{max}$  condition, verifying the feasibility discussed in Section 2.2. As shown in the 270× SEM image of Test 18, the powders produced have two typical surfaces. The side in contact with the diamond tool is relatively smooth, while the reverse shows the shear bands from the machining process. Overall, the produced powders are discrete and of relatively consistent size.

Notably, the morphology of produced powders from Test 1 is ribbonshaped, where the dimension of the width direction is significantly more than the length direction, as shown in Fig. 8(b). However, the predicted length and

11 models of ul	11.6410 Hz trasonic tool and workpiece.	0.5820 mm/s	4 μm
12	11.6410 Hz	0.5820 mm/s	6 μm
13	11.6410 Hz	0.5820 mm/s	8 μm
14	11.6410 Hz	0.5820 mm/s	10 μm
15	5.8200 Hz	0.2910 mm/s	6 μm
16	9.3128 Hz	0.4658 mm/s	6 μm
17	17.4616 Hz	0.8730 mm/s	6 μm
18	23.4640 Hz	1.1842 mm/s	6 μm

Parameters of experiments for powder production.

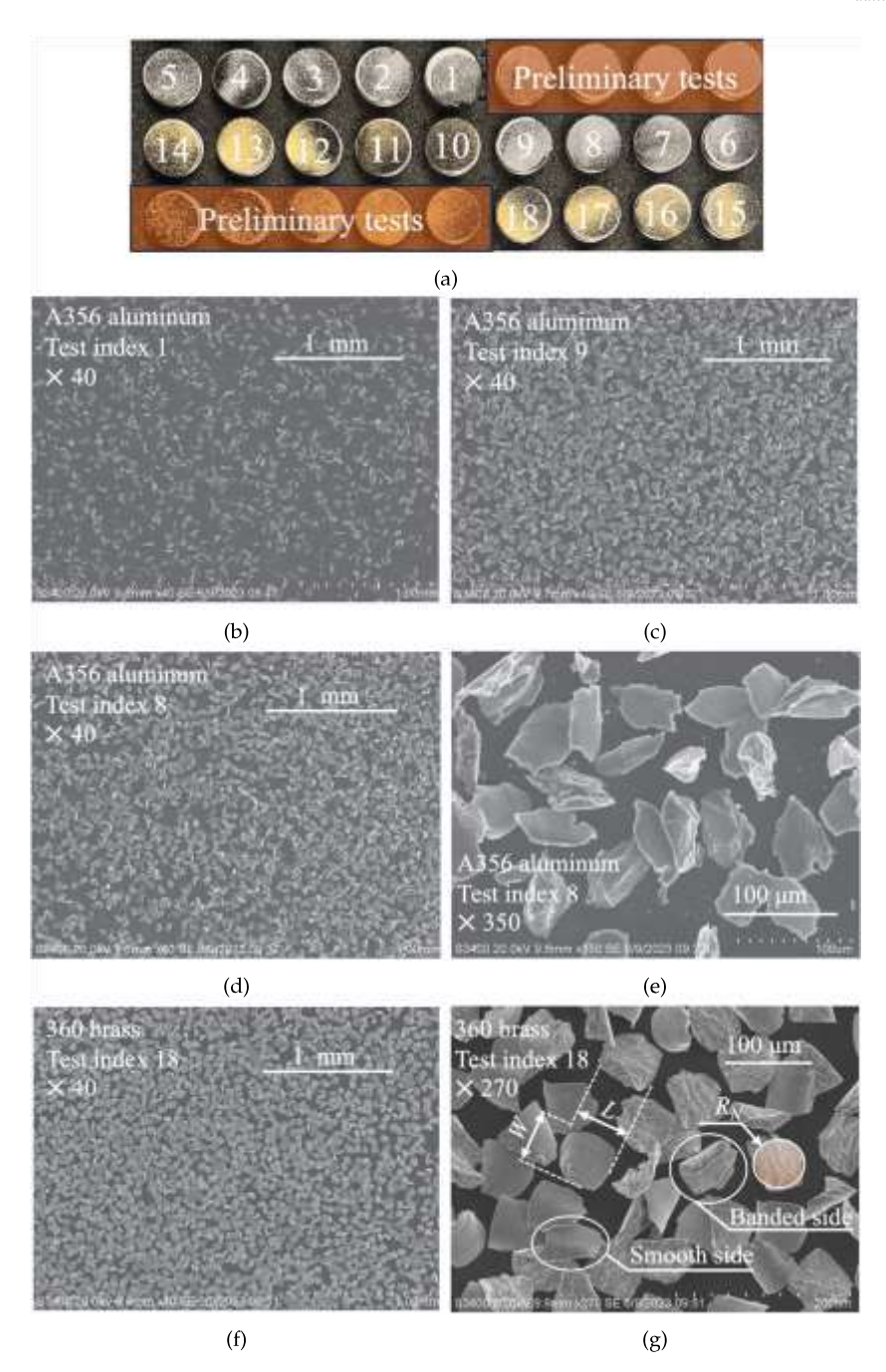


Fig. 8. (a) Collected samples powders for comparison of SEM; 40× SEM images of A356 aluminum powders of different morphology generated in Test (b) 1 and (c) 9; (d) 40× and (e) 350× SEM images of A356 aluminum powders generated in Test 8; (f) 40× and (g) 270× SEM images of 360 brass powders generated in Test 18.

 $L_0$  while the powder thickness is increases to H from  $H_0$ . As shown in Fig. 9(a), a dimple with length  $L_0$  and depth  $H_0$  corresponds to a generated powder with length L and thickness H, where  $L < L_0$  and  $H > H_0$ . Here, an overall shear ratio  $\gamma$  is used to characterize the ratio of  $(L_0, L)$  and  $(H_0, H)$ . Due to the consistency of the machined dimples during the cutting process, the overall shear ratio  $\gamma$  can be regarded as a constant if process parameters are unchanged. To calibrate the effect of the shear deformation, the length and width of the selected produced powders from all the tests in Table 2 were measured. We chose the average measurement of five flat-lying powders from each of the 270× SEM images. The length and width of the powders were measured manually using ImageJ. With the experimentally measured length of each test, the overall shear ratio can be calculated by a regression directly.

The overall shear ratio  $\gamma$  of for A356 aluminum and 360 brass was calculated to be 0.368 and 0.382, respectively. The comparison of predicted deformed

length  $\gamma Z_0$  and experimental results are shown in Fig. 9(c), where the comparison of predicted and experimentally obtained width is shown in Fig. 9(d). As shown in Fig. 9(c), Z increases with both DOC and D, which does not exceed  $\gamma D$  as discussed in Section 2.2. The measured result keeps a similar trend while the value deviates from the predicted value by 7.4% (A356 Al) and 14.5% (360 brass) on average. In Fig. 9(c), W increases with DOC as predicted while fluctuating as dimple gap D changes, which is independent of D

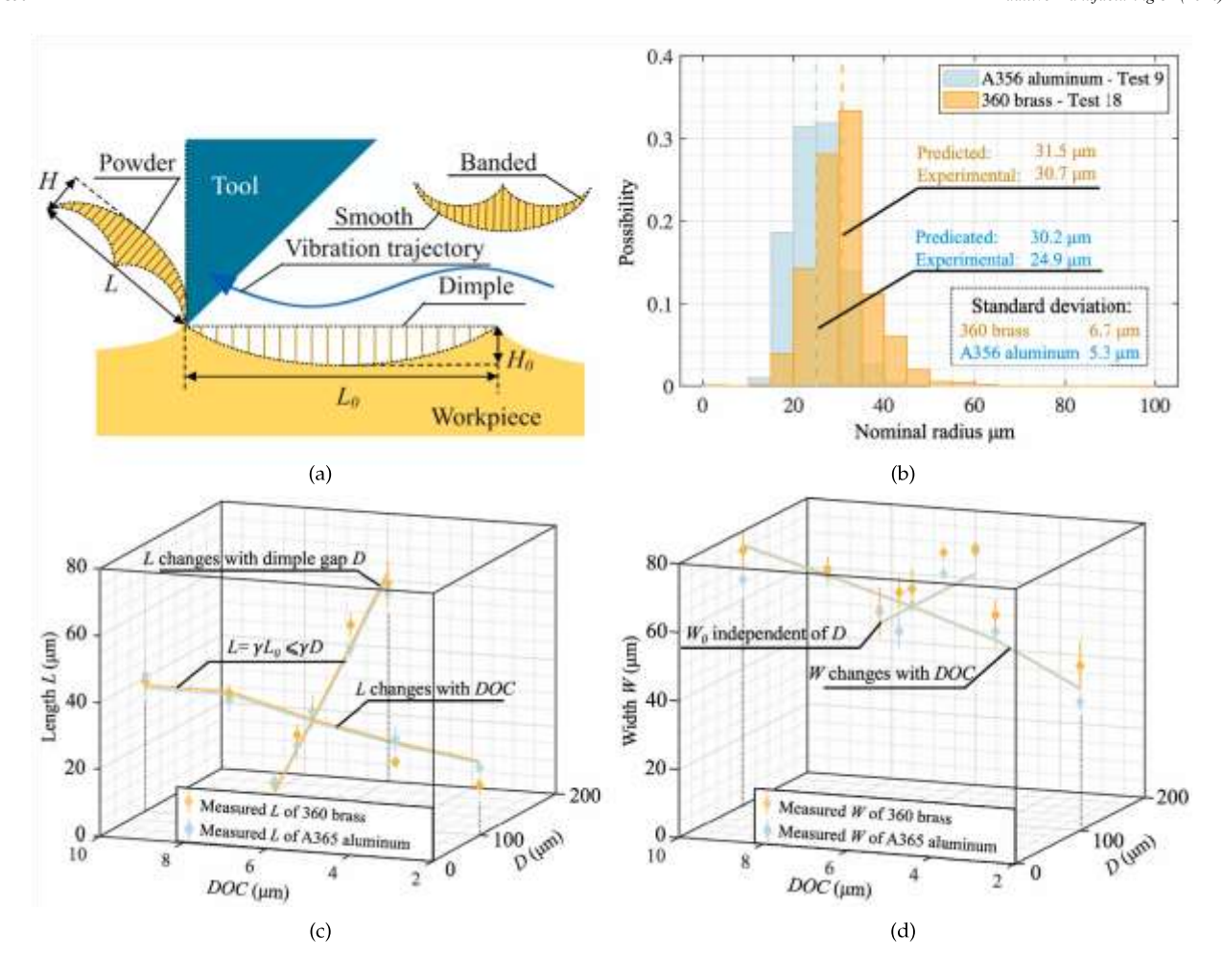


Fig. 9. (a) Shear deformation during powder generation; (b) distribution of nominal radius of produced powders from Test 9 and 18; comparison of predicted and experimental result of (c) length and (d) width.

3.2. Scalable powder generation and collection

as predicted. The prediction errors on the width are 6.9% and 8.8% for A356 aluminum and 360 brass, respectively.

According to the SEM images of Fig. 8(f), the morphology of the powders from Test 18 are of similar length and width, while the undeformed morphology is long ribbon-shaped chips. This indicates that the calibration of the shear deformation needs to be taken into consideration when producing powders of desired morphology. In addition, according to the calculation result, the predicted length and width of Test 18 are calculated to be  $60 \times 60 \ \mu m$ , which are potentially more suitable for the additive manufacturing process because of better symmetry.

Additionally, to characterize the size consistency of generated powders, the nominal radius of produced powders is characterized, as shown in Fig. 8(g). The nominal radius is the radius of the circle with the equivalent area of the powder in irregular shapes. The areas of powders in the 40× images of Tests 9 and 18 are detected and measured by *ImageJ*. The distribution of the nominal radius is shown in Fig. 9(b). The average nominal radius of the A356 aluminum powder is relatively smaller than that of the 360 brass, probably due to the minor damage to the produced powders. Also, some inconsistencies in the nominal radius are due to the orientation of the powders in the image, as the powders are not all lying flat as assumed. Overall the standard deviations of the nominal radius are 5.3  $\mu$ m and 6.7  $\mu$ m for Test 9 and Test 18, indicating area variation of 3.2% and 4.6%, respectively.

Scalable powder generation is required to produce the volumes of powder required for additive manufacturing. To enable this scalable production, an automated collection system is designed, consisting of a shroud around the workpiece, a 3D-printed centrifugal separator, a commercial vacuum cleaner, and a collection chamber. The separator is affixed directly to the spindle headstock, and the shroud is connected to the separator. The shroud itself is split into two halves for assembly and surrounds the entirety of the machined workpiece, only opening to the front near the ultrasonic tool. Air moves from near the tool into the shroud, capturing airborne powders, then proceeds through the separator where powders become separated from the airstream by density due to centrifugal motion [35,36]. The remaining clean air proceeds toward the vacuum port through a final filter. At the base of the separator, the collection chamber includes a grounding wire to reduce static electricity buildup in the plastic container. A section view of the powder collection system is shown in Fig. 10(a).

With the collection system, 94 g of A356 aluminum powders were collected, and the collection rate (the mass of collected powders divided by the mass of material cut off) is 89%. The production rate was 1.17 mm<sup>3</sup>/s, which corresponds to 11.4 g/h for aluminum and 37.43 g/h for brass. To further improve the production efficiency of the proposed method, a concept of parallel production shown in Fig. 10(b) could be applied. The solution in Fig.

production time are captured, some of which are shown in Fig. 11(a). The SEM images of the tool edge before and after the production process are shown in Fig. 11(b). The previously unbroken cutting edge is chipped and worn after the process.

When the production process begins with an unbroken tool edge, powders with sharp and clear contours are generated. The powders produced show an

**Table 3**Parameters of powder production and powder collection test.

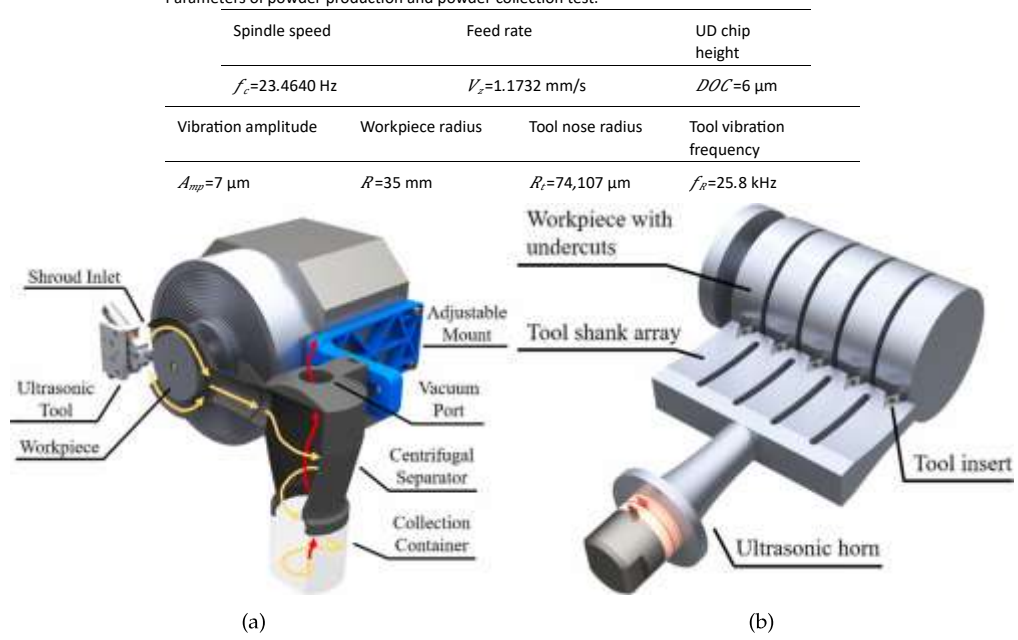


Fig. 10. (a) Section view of the collection system; (b) concept of a parallel production solution with a parallel process head.

10(b) combines multiple tools on one single ultrasonic horn, realizing parallel machining processes. Several tool inserts on the tool shank array cut the workpiece simultaneously, each tool replicating the proposed technique with the same production rate. The undercut on the workpiece divides the machined surface into separate areas for each tool, avoiding unpredictable powder generation on overlapped areas. Each tooltip cuts one cylindrical surface only, avoiding any tool alignment requirement between tools. This scalable approach for parallel production multiplies the production rate by the number of tool tips, potentially bringing the production rate of aluminum powders up to hundreds of grams per hour. This parallel production solution is mainly applicable to the proposed cylindrical turning approach since the tool vibration is normal to the machined surface, and the dimple gap is kept constant on each tool.

#### 3.3. Powder validation over relatively long-duration production

The proposed process requires a diamond tool to cut with over 10 m/s cutting speed without lubricant (for the requirement of vacuumbased powder collection), which is a strenuous working condition for the diamond tool. Thus, the change of surface condition and morphology over time induced by tool wear or possible thermal effect is validated in this section in addition to the bulk density and flowability tests of the produced powders. It is concluded that the produced powders remain consistent in dimensions during relatively long-time production while the morphology shows observable morphology change due to tool wear. The experimental details are as follows:

Using the process conditions listed in Table 3 and the diamond tool of nose radius of 74  $\mu$ m with an initially undamaged tool edge, we generated 60 g of A356 aluminum powders over 6.5 h of effective cutting time (excluding retraction time). The process starts with the A356 cylindrical workpiece of R=35 mm, and 0.3 mm of material is cut off in the radial direction every 30 min. The powder is sampled using carbon tapes every 30 min during the process. SEM images of different sections of the produced powders through the

asymmetric ribbon-like morphology. Each powder has a curved smooth face and a banded face with ridges as predicted in Section 2.2. The side face of the powders is curved due to the shear deformation during the machining process, forming a "moon-shaped" section view. As the production process proceeds, defects begin to appear on the smooth face of the powders. As the tool wear intensifies, defects on the smooth surface gradually evolve into increasingly obvious fringes. The interface in the long direction of the powder gradually changes from a clear quadrilateral contour to an approximate polygonal shape without a clear contour. However, the length and width, defined by the longest and widest points of the powder, remain approximately constant, which is further verified by measurement. This trend of morphology transition can be partially explained by the simulation result in Fig. 11(c). If the tool edge is worn and assumed to have a flat tip, the corresponding powders produced are predicted to become irregular, as the experiments present, while keeping consistent dimensions. Also, the side face of the produced powders converges to a curved "moon" shape without significant change in the powder thickness until the production process ends. Overall, the produced powders remain discrete with ribbon-shaped morphology and relatively consistent dimensions over long-duration production, while the contour of the powders becomes irregular due to tool wear. Thus, the powders can still be produced by a partially chipped/worn tool, and tool relapping is optional, depending on the desired powder. In addition, the tool life can potentially be improved by using a negative rake angle or designing a collection process where lubricant can be applied.

The dimensions of the powders sampled at different times over the total 6.5 h are measured with five individual measurements on the captured SEM images. The measured length, width, and thickness (measured at the thickest point on the side view) are shown in Fig. 12. It can be concluded that even though the morphology changed due to tool wear, the measured length of the powder does not show observable change, while the width decreases by a small portion due to portions of the powder torn off during the machining process. Also, the standard deviation of the length and width shows an increasing trend

due to different degrees of tool wear. The thickness of the produced powders is lower than the  $Hd\gamma$  because the shear deformation not only contributes to

the thickness change but also twists the powder to the aforementioned "moon" shape. Thus, the aspect ratio, which

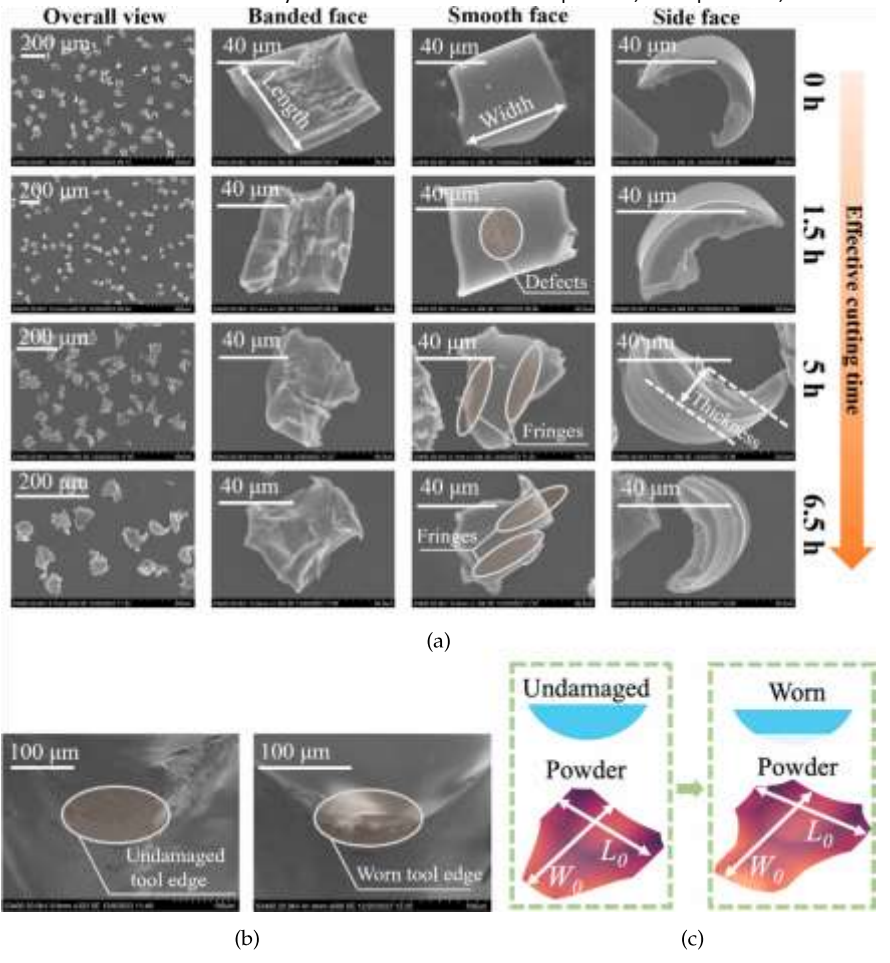


Fig. 11. (a) Exemplary SEM images of sampled powders through the production time; (b) SEM images of the tool cutting edge before and after the powder production, respectively; (c) the transition of powder morphology induced by tool wear predicted by simulation.

**Table 4** Packing density and flowability of the powders.

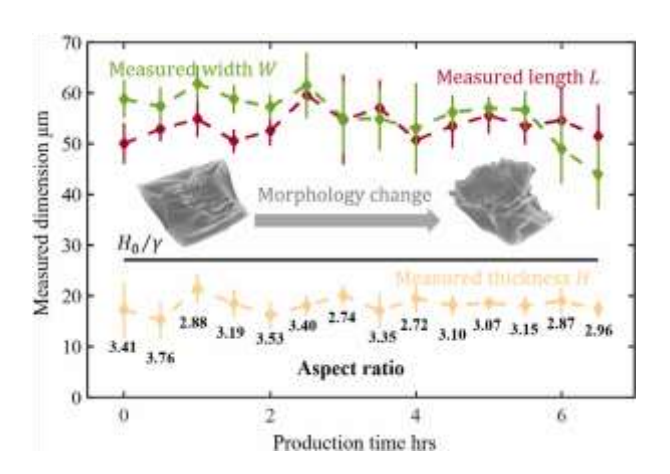
	Bulk density	Apparent density	Hall flowability	Angle of repose
Produced powders	0.79 gcm <sup>-3</sup>	30%	_	42.5 deg
Commercial powders	1.50 gcm <sup>-3</sup>	57%	67.9 s/50 g	29.9 deg

is the longest dimension between length and width divided by the thickness of the powder, cannot be directly estimated by using the overall shear ratio  $\gamma$ . Here, the experimental aspect ratio calculated using the measurement is listed in Fig. 12. The average aspect ratio of the whole production process is 3.15.

Furthermore, the bulk density and the flowability of the produced powder are tested with comparison to commercial well-filtered fine spherical aluminum powders made by gas atomization (see Table 4). The SEM image of the commercial powder is shown in Fig. 13(a), which shows fine spherical powders with diameters ranging from 20 to 60  $\mu m$ . The bulk density of the powders is measured using the ASTMB417 standard. The apparent density (ratio between the bulk density and the material density) of the produced powder is 30%, which is lower than the commercial powders but comparable with some other irregular powders [37,38] and water-atomized powders [39] used in additive manufacturing.

Also, the flowability of the produced powders is characterized as "fair" [40] with a comparable angle of repose to other non-spherical aluminum powders [41]. When testing the flowability using the ASTMB213 standard, the produced

powder does not flow freely in the Hall funnel without applied taps, which is also observed in existing tests of irregular aluminum powder [41]. Thus, we use the measurement of the



 $\textbf{Fig. 12.} \ \ \textbf{Measurement of powder dimensions and aspect ratio via production time.}$ 

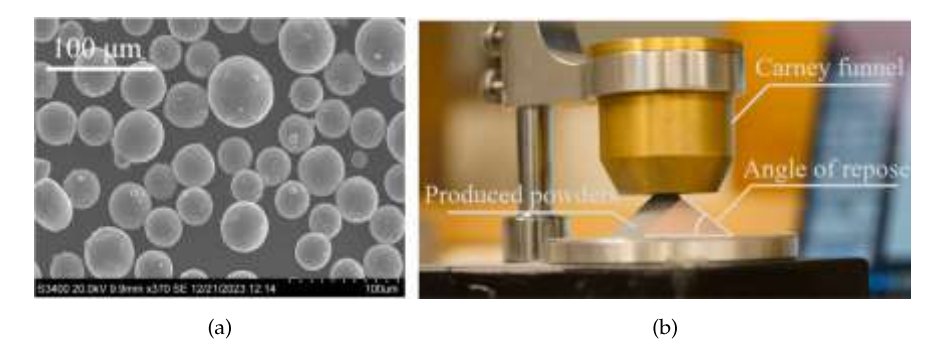


Fig. 13. (a) The SEM image of commercial powders; (b) the measurement of flowability by angle of repose.

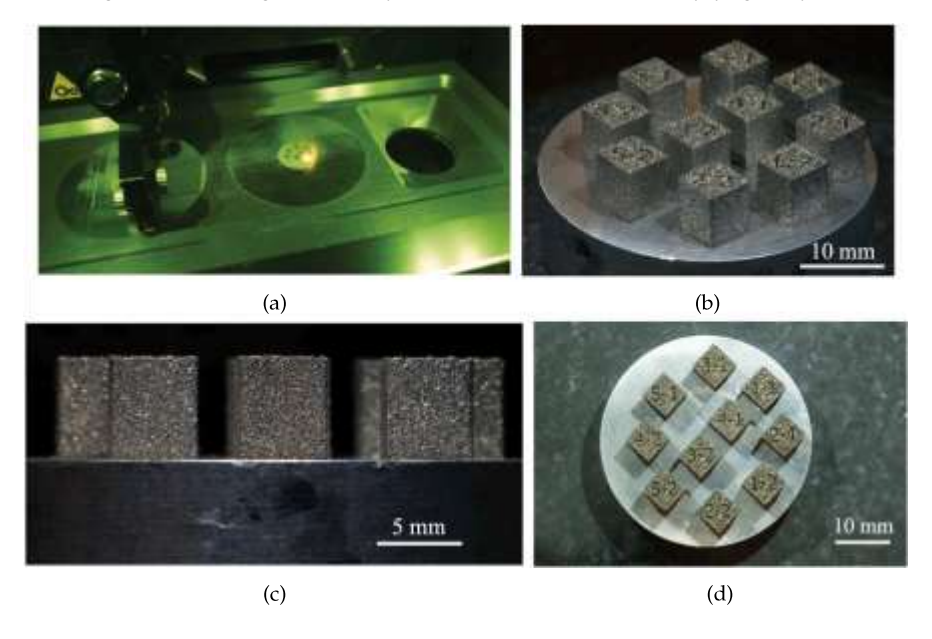


Fig. 14. (a) Image of L-PBF printing experiment; (b) actual 3D printed test blocks fabricated by L-PBF using A356 powders; the (c) side view and (d) top view of printed prisms. angle of repose as a reference for flowability [25]. Here, the method of the fixed funnel [42] is used, and the corresponding setup is shown in Fig. 13(b). The powder flows out of the Carney funnel and forms a pile on the glazed paper surface until the flow of the powder is blocked by the built-up pile. The angle of repose is determined by the ratio between the well-calibrated height of the funnel and the diameter of the powder pile minus the diameter of the funnel. The measured angle of repose is 42.5 deg, which is categorized as "fair" flowability [40], while that of the commercial powder is categorized as "excellent". The flowability of powders produced by the process can potentially improved by the design of cutting parameters and tool geometry in future studies.

# 3.4. Laser powder bed fusion (L-PBF) with produced powders

In this section, we demonstrate the printing compatibility of produced powders by using L-PBF. By using the process conditions listed in Table 3 and the other diamond tool of nose radius of 107 µm, we have additionally generated 34 g of A356 aluminum powders with lateral dimensions around 60  $\mu m$  by 60  $\mu m$ . Here, the layer thickness of L-PBF experiments was set to 20  $\mu m$ .

We used a commercial L-PBF machine (Sisma MySint100) with a 1070 nm fiber laser with a spot size of 55  $\mu m$  and maximum laser power of 200 W. Ten rectangular prisms with a size of  $5 \times 5 \times 6$  mm were printed under Ar atmosphere, and the following parameters were used: laser power of 150–200 W, scanning speed of 1200-1600 mm/s, hatch spacing of 100 µm, and layer thickness of 20 µm, also listed in Table 5. A bidirectional scanning strategy was used with 90° rotation between

Table 5 Parameters of L-PBF experiments.

Hatch spacin	g Layer thickness	Laser spot size	Substrate preheating
100 μm	20 μm	55 μm	No
	Sample index	Laser power	Scan speed
•	1-1, 1-2	200 W	1400 mm/s
	2-1, 2-2	175 W	1200 mm/s
	3-1, 3-2	175 W	1400 mm/s
	4-1, 4-2	175 W	1600 mm/s
	5_1 5_2	150 W/	1400 mm/s

layers, with a single contour. The sample printing process is shown in Fig. 14(a). The powders were spread with a commercial rubber recoater provided by Sisma. The printing results are shown in Fig. 14(b). The side view of the printed blocks is shown in Fig. 14(c). No major defects show up on the side of the printed blocks, demonstrating the feasibility of producing powders on printing using thin layer thickness (20  $\mu$ m). The top view of the printed blocks is shown in Fig. 14(d) where all the samples show clear texts of the sample index. The quality of the surface finish is improved from 1 to 5 in sequence according to visual inspection, indicating that the parameters used for 5-1 and 5-2 are

currently the optimal printing setting for produced powders. Nevertheless, this is the first result to demonstrate the feasibility to use mechanically machined uniform powders for laser powder bed fusion.

To further study the microstructure and properties of the printed prisms,

material sample due to the coarse microstructure. Indents were made to avoid obvious porosity, and 10–12 measurements were taken per sample. The results of microhardness measurements for the L-PBF and raw A356 samples are shown in Fig. 15(b). The average hardness of each sample and the

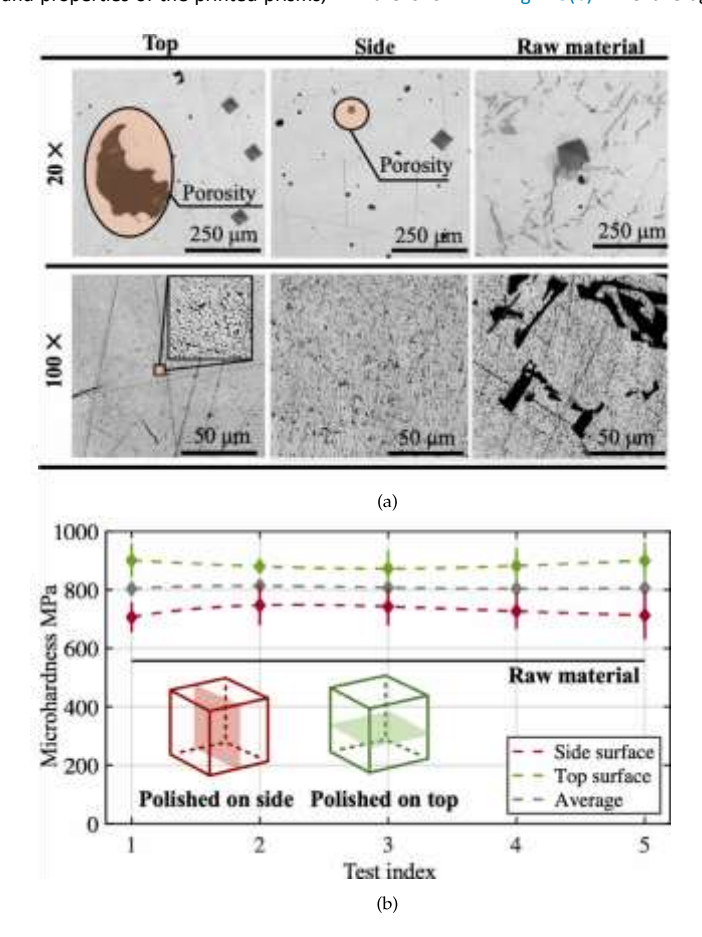


Fig. 15. (a) 20× and 100× optical microscopy of polished prisms made of L-PBF and polished raw material feedstock; (b) results of microhardness measurement.

tests. The top (the surfaces with labels) and side faces (the surfaces without labels) of the printed prisms and the raw material feedstock are polished to a mirror finish using 0.06 µm colloidal silica. The microscopic images of the surface are captured by a 3D laser confocal microscope (OLS5000, Olympus, USA). The images from samples 5-1 and 5-2 and the raw material feedstock are shown in Fig. 15 as an example. The 20× images show porosity in the printed prisms, along with the hardness indents. In the 20× images of the top surface, large pores with sizes up to hundreds of microns, possibly induced by lack of fusion in the powder bed, are found. However, the microscopic images of the side surface contain only smaller pores, which have circular boundaries and are tens of microns in diameter. Also, the 100× images are captured in areas without visible major porosities, the contrast of which is adjusted for better presentation of the eutectic Si phases. For the 100× image of raw material, a large number of needle-like eutectic Si precipitates were found, consistent with typical cast A356 microstructures [43]. However, in the samples produced by L-BPF, the same precipitates are highly refined, consistent with faster cooling rates occurring in the L-PBF process [44]. Thus, while these parts contain large pores, the microstructure between the pores is visually consistent with that observed in similar, LPBF-processed Al-Si-based alloys

we capture optical microscopy images and conduct Vickers microhardness

For further comparison of the mechanical properties, Vickers microhardness tests are conducted on the polished prisms and raw material. A 200-gram-force load is applied to the L-PBF samples, and a 500-gramforce load is applied to the raw material sample with a dwell time of 10 s, forming micro indents as shown in Fig. 15(a). The higher load was chosen for the raw

[45].

corresponding standard deviation are calculated. The overall average microhardness of the L-PBF samples is 807.3 MPa, which is 45% higher than that of the raw material. The higher hardness of the L-PBF samples is consistent with the finer solidification microstructure, which is again due to the faster cooling rates in the L-PBF process compared to conventional casting. In addition, the hardness is higher on the top surface of the L-PBF-printed parts than on the side surface. This anisotropy effect is also observed in previous studies on a similar L-PBF processed AlSi10Mg alloy, where the highly directional thermal gradient results in anisotropy in both the microstructure and resulting mechanical properties [46,47]. There is a mild trade-off trend when considering the hardness of the top and side surfaces with respect to process parameters, suggesting slight variations in the degree of anisotropy with respect to the processing conditions. However, there is no significant effect of the laser process parameters when considering the microhardness of the top and sides averaged together. Overall, these results indicate enhanced but anisotropic microhardness in the printed prisms compared to the raw material, which is common to similar L-PBF processed Al-Si-based alloys.

# 4. Conclusion

This work presents a new solid-state fabrication technique to produce uniform and micron-sized metal powders for additive manufacturing applications. By collecting discrete chips resulting from ultrasonic vibration machining, we demonstrate the feasibility of generating consistent powders with tight dimensional tolerance, the ability to control powder geometry and

good efficiency. The major technical contributions of the study can be summarized as:

 A tool path design strategy to achieve consistent powder dimensions despite the evolving machined topography over multiple cuts is proposed;

# **CRediT authorship contribution statement**

Yaoke Wang: Writing – original draft, Visualization, Validation, Methodology, Investigation. Malachi Landis: Writing – review & editing, Visualization, Validation, Resources, Methodology. Clement Ekaputra: Writing

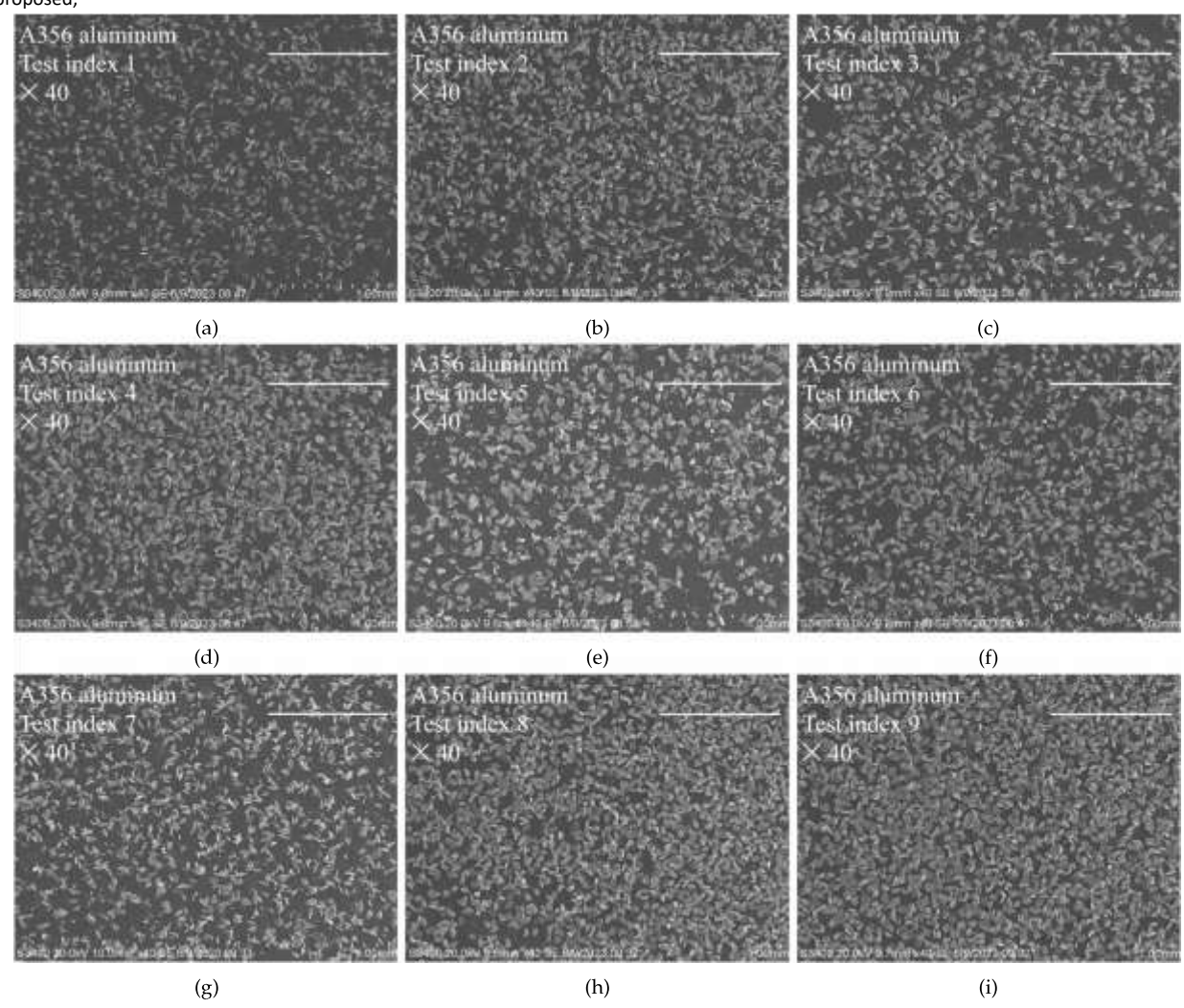


Fig. A.1. Exemplary SEM results of produced A356 aluminum powders from (a) Test 1 to (i) Test 9. Scale bar = 1 mm.

- 2. An efficient powder collection system and parallel production solution for the proposed technique are introduced;
- The short-ribbon-shaped powders are generated with tunable lengths and widths. Both dimensions can be adjusted from tens of microns to hundreds of microns depending on the printing requirements;
- 4. The first L-PBF printing result using mechanically machined A356 aluminum powders using only 20 μm layer thickness is presented. The printed parts show refined microstructures and increased microhardness compared to the raw material.

This work is expected to illuminate a new route for sustainable and low-cost manufacturing of high-quality metal powders. One last note is regarding the broader feasibility. Since the process only requires a CNC system with a programmable spindle axis and an ultrasonic actuator, the process can be utilized as a quick on-site fabrication solution of powders of variable material and dimensions without the need for post-processing or further powder refinement.

review & editing, Validation, Resources. Valeria Vita: Validation, Resources.
 Ping Guo: Writing – review & editing, Supervision, Funding acquisition, Conceptualization.

# **Declaration of competing interest**

The authors declare that they have no known competing financial interests or personal relationships that could have appeared to influence the work reported in this paper.

# Data availability

Data will be made available on request.

### Acknowledgments

This research was supported by the National Science Foundation under Grant number CMMI-2216298 and EEC-2133630. This work made use of the MatCI Facility supported by the MRSEC program of the National Science Foundation (DMR-1720139) at the Materials Research Center of Northwestern

University. This work made use of the EPIC facility of Northwestern University's NUANCE Center, which has received support from the SHyNE Resource (NSF ECCS-2025633), the IIN, and Northwestern's MRSEC program (NSF DMR-2308691).

#### **Appendix**

The exemplary SEM images of produced powders are listed in Fig. A.1 for A356 aluminum and in Fig. A.2 for 360 brass, respectively.

[5] I.E. Anderson, E.M. White, R. Dehoff, Feedstock powder processing research needs for additive manufacturing development, Curr. Opin. Solid State Mater.

Sci. 22 (1) (2018) 8-15, http://dx.doi.org/10.1016/j.cossms.2018.01.002.

- [6] S. Lagutkin, L. Achelis, S. Sheikhaliev, V. Uhlenwinkel, V. Srivastava, Atomization process for metal powder, Mater. Sci. Eng., A 383 (1) (2004) 1–6, http://dx.doi.org/10.1016/j.msea.2004.02.059.
- [7] M. Tsirlis, N. Michailidis, Optimization of aluminium powder production through a novel ultralow pressure gas-atomization method, CIRP Ann. 71 (1) (2022) 141–144, http://dx.doi.org/10.1016/j.cirp.2022.04.031.
- [8] M. Wei, S. Chen, M. Sun, J. Liang, C. Liu, M. Wang, Atomization simulation and preparation

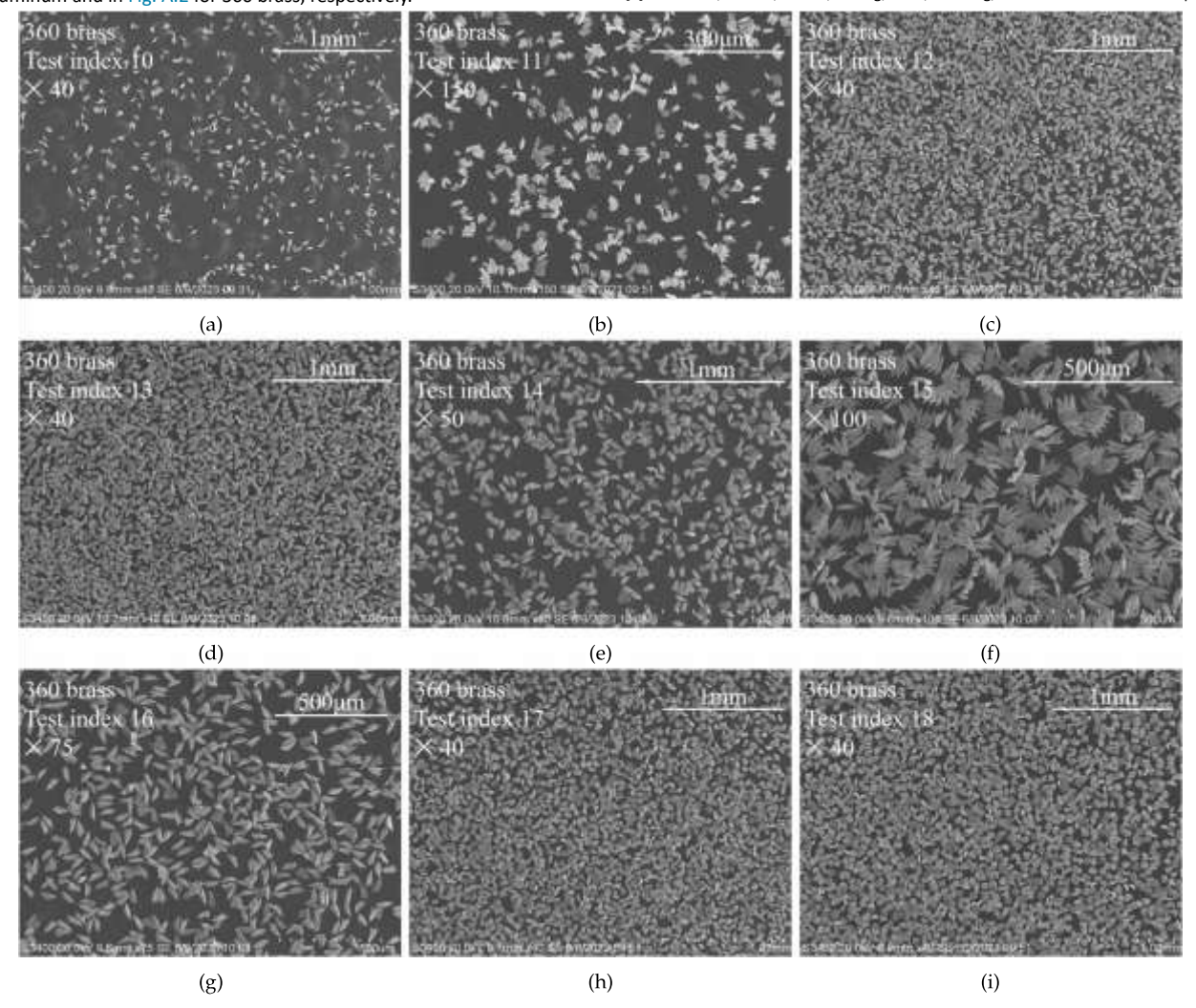


Fig. A.2. Exemplary SEM results of produced 360 brass powders from (a) Test 10 to (i) Test 18.

# References

- [1] M.K. Thompson, G. Moroni, T. Vaneker, G. Fadel, R.I. Campbell, I. Gibson, A. Bernard, J. Schulz, P. Graf, B. Ahuja, et al., Design for additive manufacturing: Trends, opportunities, considerations, and constraints, CIRP Ann. 65 (2) (2016) 737–760, http://dx.doi.org/10.1016/j.cirp.2016.05.004.
- [2] Y. Kakinuma, M. Mori, Y. Oda, T. Mori, M. Kashihara, A. Hansel, M. Fujishima, Influence of metal powder characteristics on product quality with directed energy deposition of inconel 625, CIRP Ann. 65 (1) (2016) 209–212, http://dx.doi.org/ 10.1016/j.cirp.2016.04.058.
- [3] E. Garboczi, N. Hrabe, Particle shape and size analysis for metal powders used for additive manufacturing: Technique description and application to two gasatomized and plasmaatomized Ti64 powders, Addit. Manuf. 31 (2020) 100965, http://dx.doi.org/10.1016/j.addma.2019.100965.
- [4] X. Wang, H. Yang, X. Yu, C. Hu, J. Hu, R. Li, Y. Zhang, Functional metal powders: Design, properties, applications, and prospects, Mater. Sci. Eng., B 280 (2022) 115708, http://dx.doi.org/10.1016/j.mseb.2022.115708.

- of 24CrNiMoY alloy steel powder using VIGA technology at high gas pressure, Powder Technol. 367 (2020) 724–739, http://dx.doi.org/10.1016/j.powtec.2020.04.030.
- [9] K. Kassym, A. Perveen, Atomization processes of metal powders for 3D printing, Mater. Today Proc. 26 (2020) 1727–1733, http://dx.doi.org/10.1016/j.matpr. 2020.02.364.
- [10] T. Fedina, J. Sundqvist, J. Powell, A.F. Kaplan, A comparative study of water and gas atomized low alloy steel powders for additive manufacturing, Addit. Manuf. 36 (2020) 101675, http://dx.doi.org/10.1016/j.addma.2020.101675.
- [11] M. Abdelwahed, S. Bengtsson, R. Casati, A. Larsson, S. Petrella, M. Vedani, Effect of water atomization on properties of type 4130 steel processed by L-PBF, Mater. Des. 210 (2021) 110085, http://dx.doi.org/10.1016/j.matdes.2021.110085.
- [12] G. Chen, S. Zhao, P. Tan, J. Wang, C. Xiang, H. Tang, A comparative study of Ti-6Al-4V powders for additive manufacturing by gas atomization, plasma rotating electrode process and plasma atomization, Powder Technol. 333 (2018) 38–46, http://dx.doi.org/10.1016/j.powtec.2018.04.013.
- [13] M. Entezarian, F. Allaire, P. Tsantrizos, R. Drew, Plasma atomization: A new process for the production of fine, spherical powders, Jom 48 (1996) 53–55, http://dx.doi.org/10.1007/BF03222969.

- [14] P. Sungkhaphaitoon, T. Plookphol, S. Wisutmethangoon, Design and development of a centrifugal atomizer for producing zinc metal powder, Int. J. Appl. Phys. Math. 2 (2) (2012) 77, http://dx.doi.org/10.7763/IJAPM.2012.V2.58.
- [15] M.A. Jackson, J.D. Morrow, D.J. Thoma, F.E. Pfefferkorn, A comparison of 316 L stainless steel parts manufactured by directed energy deposition using gas-atomized and mechanically-generated feedstock, CIRP Ann. 69 (1) (2020) 165–168, http://dx.doi.org/10.1016/j.cirp.2020.04.042.
- [16] J.W. Murray, A. Speidel, A. Jackson-Crisp, P.H. Smith, H. Constantin, A.T. Clare, Unprocessed machining chips as a practical feedstock in directed energy deposition, Int. J. Mach. Tools Manuf. 169 (2021) 103803, http://dx.doi.org/10. 1016/i.ijmachtools.2021.103803.
- J. Huang, Y. Wu, H. Ye, Ball milling of ductile metals, Mater. Sci. Eng., A 199
   (2) (1995) 165–172, http://dx.doi.org/10.1016/0921-5093(94)09715-1.
- [18] L. Wei, S. Abd Rahim, M. Al Bakri Abdullah, A. Yin, M. Ghazali, M. Omar, O. Nemeş, A. Sandu, P. Vizureanu, A. Abdellah, Producing metal powder from machining chips using ball milling process: A review, Materials 16 (13) (2023) 4635, http://dx.doi.org/10.3390/ma16134635.
- [19] B. Fullenwider, P. Kiani, J.M. Schoenung, K. Ma, Two-stage ball milling of recycled machining chips to create an alternative feedstock powder for metal additive manufacturing, Powder Technol. 342 (2019) 562–571, http://dx.doi. ore/10.1016/i.powtec.2018.10.023.
- [20] A. Bor, B. Jargalsaikhan, K. Uranchimeg, J. Lee, H. Choi, Particle morphology control of metal powder with various experimental conditions using ball milling, Powder Technol. 394 (2021) 181–190, http://dx.doi.org/10.1016/j.powtec.2021. 08.053.
- [21] H. Li, J. He, Q. Sun, S. Wang, Effect of the environment on the morphology of Ni powder during high-energy ball milling, Mater. Today Commun. 25 (2020) 101288, http://dx.doi.org/10.1016/j.mtcomm.2020.101288.
- [22] C. Carreño-Gallardo, I. Estrada-Guel, C. López-Meléndez, E. Ledezma-Sillas, R. Castañeda-Balderas, R. Pérez-Bustamante, J.M. Herrera-Ramírez, B4C particles reinforced Al2024 composites via mechanical milling, Metals 8 (8) (2018) 647, http://dx.doi.org/10.3390/met8080647.
- [23] Y. He, A. Hassanpour, A.E. Bayly, Combined effect of particle size and surface cohesiveness on powder spreadability for additive manufacturing, Powder Technol. 392 (2021) 191–203. http://dx.doi.org/10.1016/i.powtec.2021.06.046.
- [24] C. Meier, R. Weissbach, J. Weinberg, W.A. Wall, A.J. Hart, Critical influences of particle size and adhesion on the powder layer uniformity in metal additive manufacturing, J. Mater Process. Technol. 266 (2019) 484–501, http://dx.doi. org/10.1016/i.jmatprotec.2018.10.037.
- [25] X. Sun, M. Chen, T. Liu, K. Zhang, H. Wei, Z. Zhu, W. Liao, Characterization, preparation, and reuse of metallic powders for laser powder bed fusion: a review, Int. J. Extreme Manuf. 6 (1) (2023) 012003, http://dx.doi.org/10.1088/26317990/acfbc3.
- [26] J. Mann, C. Saldana, S. Chandrasekar, W. Compton, K. Trumble, Metal particulate production by modulation-assisted machining, Scr. Mater. 57 (10) (2007) 909–912, http://dx.doi.org/10.1016/j.scriptamat.2007.07.025.
- [27] R. Garg, H.S. Dhami, P.R. Panda, K. Viswanathan, Evaluating gas-driven flow mechanics of non-spherical powders for directed energy deposition, J. Manuf. Process. 99 (2023) 260–271, http://dx.doi.org/10.1016/j.jmapro.2023.04.057.
- [28] J.H. Martin, J.E. Barnes, K.A. Rogers, J. Hundley, D.L. LaPlant, S. Ghanbari, J.-T. Tsai, D.F. Bahr, Additive manufacturing of a high-performance aluminum alloy from cold mechanically derived non-spherical powder, Commun. Mater. 4 (1) (2023) 39, http://dx.doi.org/10.1038/s43246-023-00365-4.
- [29] S.P. Narra, Z. Wu, R. Patel, J. Capone, M. Paliwal, J. Beuth, A. Rollett, Use of non-spherical hydride-dehydride (HDH) powder in powder bed fusion additive manufacturing, Addit. Manuf. 34 (2020) 101188, http://dx.doi.org/10.1016/j. addma.2020.101188.
- [30] M. Asherloo, J. Hwang, R. Leroux, Z. Wu, K. Fezzaa, M. Paliwal, A.D. Rollett, A. Mostafaei, Understanding process-microstructure-property relationships in laser powder bed fusion of non-spherical Ti-6Al-4V powder, Mater. Charact. 198 (2023) 112757, http://dx.doi.org/10.1016/j.matchar.2023.112757.
- [31] J. Guzmán, R. de Moura Nobre, E.R. Nunes, D.L. Bayerlein, R.B. Falcão, E. Sallica-Leva, J.B.F. Neto, H.R. Oliveira, V.L. Chastinet, F.J. Landgraf, Laser powder bed fusion parameters to produce high-density ti–53% nb alloy using irregularly shaped powder from hydride-dehydride (HDH) process, J. Mater. Res.
  Technol. 10 (2021) 1372–1381. http://dx.doi.org/10.1016/j.imrt.2020.12.084.
- [32] P. Guo, Y. Lu, P. Pei, K.F. Ehmann, Fast generation of micro-channels on cylindrical surfaces by elliptical vibration texturing, J. Manuf. Sci. Eng. 136 (4) (2014) http://dx.doi.org/10.1115/1.4027126.
- [33] P. Guo, K.F. Ehmann, An analysis of the surface generation mechanics of the elliptical vibration texturing process, Int. J. Mach. Tools Manuf. 64 (2013) 85–95, http://dx.doi.org/10.1016/j.ijmachtools.2012.08.003.

- [34] P. Guo, K.F. Ehmann, Development of a tertiary motion generator for elliptical vibration texturing, Precis. Eng. 37 (2) (2013) 364–371, http://dx.doi.org/10. 1016/i.orecisioneng.2012.10.005.
- [35] T. Yamamoto, T. Shinya, K. Fukui, H. Yoshida, Classification of particles by centrifugal separator and analysis of the fluid behavior, Adv. Powder Technol. 22 (2) (2011) 294–299, http://dx.doi.org/10.1016/j.apt.2010.12.009.
- [36] A.S. Shinkaryov, M.V. Cherkasova, I.A. Pelevin, D.Y. Ozherelkov, S.V. Chernyshikhin, N.A. Kharitonova, A.A. Gromov, A.Y. Nalivaiko, Aluminum powder preparation for additive manufacturing using electrostatic classification, Coatings 11 (6) (2021) 629, http://dx.doi.org/10.3390/coatings11060629.
- [37] H. Zhu, J. Fuh, L. Lu, The influence of powder apparent density on the density in direct laser-sintered metallic parts, Int. J. Mach. Tools Manuf. 47 (2) (2007) 294–298, http://dx.doi.org/10.1016/i.iimachtools.2006.03.019.
- [38] J. Guzmán, R. de Moura Nobre, D.L. Rodrigues Júnior, W.A. de Morais, E.R. Nunes, D.L. Bayerlein, R. Falcao, E. Sallica-Leva, H.R. Oliveira, V.L. Chastinet, et al., Comparing spherical and irregularly shaped powders in laser powder bed fusion of Nb47Ti alloy, J. Mater. Eng. Perform. 30 (9) (2021) 6557–6567, http://dx.doi.org/10.1007/s11665-021-05916-9
- [39] A. Rogalsky, I. Rishmawi, L. Brock, M. Vlasea, Low cost irregular feed stock for laser powder bed fusion, J. Manuf. Process. 35 (2018) 446–456, http: //dx.doi.org/10.1016/j.jmapro.2018.08.032.
- [40] J. Zegzulka, D. Gelnar, L. Jezerska, R. Prokes, J. Rozbroj, Characterization and flowability methods for metal powders, Sci. Rep. 10 (1) (2020) 21004, http://dx.doi.org/10.1038/s41598-020-77974-3.
- [41] J. Kraner, J. Medved, M. Godec, I. Paulin, Characterization of non-ferrous metal powders, Mater. Tehnol. 54 (1) (2020) 149–153, http://dx.doi.org/10.17222/mit.2019.213.
- [42] L. Marchetti, C. Hulme-Smith, Flowability of steel and tool steel powders: A comparison between testing methods, Powder Technol. 384 (2021) 402–413, http://dx.doi.org/10.1016/j.powtec.2021.01.074.
- [43] S. Shabestari, F. Shahri, Influence of modification, solidification conditions and heat treatment on the microstructure and mechanical properties of A356 aluminum alloy, J. Mater. Sci. 39 (2004) 2023–2032, http://dx.doi.org/10.1023/B:JMSC.0000017764.20609.0d.
- [44] P.A. Rometsch, Y. Zhu, X. Wu, A. Huang, Review of high-strength aluminium alloys for additive manufacturing by laser powder bed fusion, Mater. Des. 219 (2022) 110779, http://dx.doi.org/10.1016/j.matdes.2022.110779.
- [45] F. Trevisan, F. Calignano, M. Lorusso, J. Pakkanen, A. Aversa, E.P. Ambrosio, M. Lombardi, P. Fino, D. Manfredi, On the selective laser melting (SLM) of the AlSi10Mg alloy: process, microstructure, and mechanical properties, Materials 10 (1) (2017) 76, http://dx.doi.org/10.3390/ma10010076.
- [46] C. Jing, H. Wei, W. Xiuzhuan, C. Songlin, Y. Zhiyi, Microstructure, porosity and mechanical properties of selective laser melted alsi10mg, Chinese J. Aeronaut. 33 (7) (2020) 2043–2054, http://dx.doi.org/10.1016/j.cja.2019.08.017.
- [47] N.T. Aboulkhair, A. Stephens, I. Maskery, C. Tuck, I. Ashcroft, N.M. Everitt, Mechanical properties of selective laser melted alsi10mg: nano, micro, and macro properties, in: 2015 International Solid Freeform Fabrication Symposium, University of Texas at Austin, 2015, URL https://hdl.handle.net/2152/89398.